Journal of Physical Chemistry C, 2015, Vol. 119 (33), pp 18877−18885
DOI: 10.1021/acs.jpcc.5b04178

Phase Structure Tuned Electrocaloric Effect and Pyroelectric Energy Harvesting Performance of $(Pb_{0.97}La_{0.02})(Zr,Sn,Ti)O_3$ Antiferroelectric Thick Films

Xihong Hao[*,1], Ye Zhao[1], and Qi Zhang[2,3]

1-School of Materials and Metallurgy, Inner Mongolia University of Science and Technology, Baotou 014010, China

2-State Key Laboratory of Advanced Technology for Materials Synthesis and Processing, Wuhan University of Technology, Wuhan 430070, Hubei, China

3-Department of Manufacturing and Materials, Cranfield University, Cranfield, Bedfordshire, MK43 0AL, UK

Abstract: In present work, (100)-oriented $(Pb_{0.97}La_{0.02})(Zr_{0.95-x}Sn_xTi_{0.05})O_3$ antiferroelectric thick films with x=0.08, 0.20 and 0.38, were successfully fabricated. These compositions are located in orthorhombic phase region, the morphotropic phase boundary (MPB), and tetragonal phase region, respectively. The effects of their phase structure on the electrocaloric effect and the pyroelectric energy harvesting behavior were investigated. A considerable temperature reduction of ΔT=13, 33, and 27 ^oC, due to the ferroelectric-antiferroelectric phase transition, was obtained at 25 ^oC in these thick films for x=0.08, 0.20, and 0.38, respectively. Moreover, a huge harvested energy density per cycle of W= 3.6, 6.8, and 4.0 J/cm^3 was also realized under the experimental condition in the thick films with x=0.08, 0.20, and 0.38, respectively. These results indicated that both the cooling performance and the pyroelectric energy harvesting in antiferroelectrics could be optimized by the proper phase structure control.

Keywords: Antiferroelectric; Thick films; Phase structure; Electrocaloric effect; Pyroelectric energy harvesting

*Corresponding author: xhhao@imust.cn; Tel: +86-472-5951572; Fax: +86-472-5951571

1. Introduction

Micron- and nano-electronic devices with high power density have been intensively used, however, the produced heat is harmful to the operational stability of the devices. Maintaining these devices operating at a constant, low temperature is a challenge. Therefore, electrocaloric cooling is drawing increasing attention because of its feasible structure, high efficient and environmentally friendly, and quite a few works have been reported [1-3]. Electrocaloric effect (ECE) is an universal phenomenon in polar materials, which refers to the isothermal entropy change (ΔS) and the adiabatic temperature change (ΔT) caused by the polarization variation under the application and removal of external electric field [4]. Assuming the Maxwell relation $\left(\frac{\partial P}{\partial T}\right)_E = \left(\frac{\partial S}{\partial E}\right)_T$, the reversible changes of ΔT and ΔS for a material of density (ρ) with molar heat capacity (C) are expressed by [5]:

$$\Delta S = -\frac{1}{\rho}\int_{E_1}^{E_2}\left(\frac{\partial P}{\partial T}\right)_E \mathrm{d}E\,, \tag{1}$$

$$\Delta T = -\frac{1}{C\rho}\int_{E_1}^{E_2} T\left(\frac{\partial P}{\partial T}\right)_E dE\,, \tag{2}$$

where T is operating temperature, P is maximum polarization at applied electric field E, E_1 and E_2 are the initial and final applied electric field, and $\left(\frac{\partial P}{\partial T}\right)_E$ is the pyroelectric coefficient at selected electric field. Physically, ECE is the reverse process of pyroelectric effect defined as the polarization change due to the temperature variation in pyroelectric materials [4]. According to Eq. (1) and (2), it could be concluded that materials having large pyroelectric effect and high breakdown field should possess good ECE.

The earliest study on ECE mainly focused on bulk ceramics forms [6-7]. However, because of the low breakdown electric field, the observed ECE of ceramics was very weak. For example, the highest ECE was only 2.5 ^{o}C in $Pb_{0.99}Nb_{0.02}(Zr_{0.75}Sn_{0.20}Ti_{0.05})_{0.98}O_3$ bulk ceramic [8]. In 2006, a giant ECE of 12 ^{o}C at 714 kV/cm were reported in 350-nm-thick $PbZr_{0.95}Ti_{0.05}O_3$ film, which inspired the research interest in ECE again [9]. As a result, over the last decade, the cooling

performance originated from ECE was widely studied and accordingly the outstanding ECE values were also achieved in some ferroelectrics (FEs) and antiferroelctrics (AFEs) thin films [10-15]. Over all, the present studies on ECE are mainly concentrated on the FE (or AFE)-paraelectric (PE) switching process, because of the large entropy change and the considerable pyroelectric effect caused by the structure phase transition. In fact, the phase transition between AFE and FE could also bring a large entropy change, and is easily realized at near room temperatures, while the phase transition of AFE/FE-PE usually occurs at high temperature. As a result, a large temperature change should also be obtained during FE-AFE transition upon the application and withdrawal of electric field, as shown in Fig. 1(a). Moreover, it was reported that the magnitude of $\left(\frac{\partial P}{\partial T}\right)_E$ was much higher from FE-AFE transition than that from FE (or AFE) to PE transition [16,17]. The first work on the ECE in AFEs was reported by Thacher in 1968, in which a temperature change of ΔT = 1.6 ^{o}C at 30 kV/cm, according to a huge electrocaloric coefficient of 0.053 K·cm/kV, was observed at 55 ^{o}C in $Pb(Zr_{0.455}Sn_{0.455}Ti_{0.09})O_3$ bulk ceramics during FE-AFE phase switching [7]. Quite recently, a giant ECE (ΔT = 53.8 ^{o}C and ΔS = 63.9 $J\cdot K^{-1}\cdot kg^{-1}$) with an electrocaloric coefficient of 0.060 K·cm/kV was also achieved at 5 ^{o}C in our previous work on 2-μm-$Pb_{0.97}La_{0.02}(Zr_{0.75}Sn_{0.18}Ti_{0.07})O_3$ AFE thick film [18].

Currently, the produced low-grade heat during the cooling and other heat sources are usually directly released to the air and wasted, which are becoming an increasing contribution to the global warming [19]. For harvesting the low-grade waste heat, the direct energy conversion technologies originated from thermoelectric and pyroelectric effect has being drawn significant attention in the past decade [20]. The study on pyroelectric energy harvesting could date back to 1960s [21-23]. Due to a low energy density per cycle (less than 10^{-4} J/cm^3), little attention was paid on pyroelectric materials in the following two decades [24]. Until 1980s, a new type of thermal-electrical cycle, which was similar to the Ericsson cycle and consisted of two isotherms and two isoelectric field processes, was introduced by Olsen and named as Olsen cycle [25-27]. Accordingly, a large energy density per cycle of 0.3 J/cm^3 was achieved in $Pb_{0.99}Nb_{0.02}(Zr_{0.68}Sn_{0.25}Ti_{0.07})_{0.98}O_3$ ceramics, which

was about one-thousand-fold larger than the previously reported values [25]. This result indicates that proper thermal-electrical cycle is a key factor to obtain good energy harvesting performance in pyroelectric materials. The Olsen cycle versus electric field-polarization (*P-E*) loops in the first quadrant was shown in Fig. 1(b). Process 1-2 is to increase the electric field isothermally at low temperature (T_L). Process 2-3 is to heat the pyroelectric materials from T_L to high temperature (T_H) at high electric field (E_H). Process 3-4 is to decrease the electric field isothermally at T_H. Process 4-1 is to cool the materials at low electric field (E_L) and the cycle is closed. The harvested thermal-electrical energy density per cycle (W) is equal to the area 1-2-3-4 between the two P-E loops at T_L and T_H operated at E_L and E_H in Fig. 1(b), and expressed as [28]:

$$W = \oint EdP, \tag{3}$$

where E is the electric field, and P the polarization. Intrigued by Olsen's work, many papers on the thermal-electrical energy harvesting of different pyroelectric materials , such as bulks FE ceramics and polymers, were reported [29-32]. Based on the reported results, it was found that the improved energy harvesting performance could be realized in the materials with large pyroelectric coefficient under high external electric fields by employing the Olsen cycle. For example, a large W value of 0.888 J/cm^3 and 1.523 J/cm^3 were obtained in $Pb_{0.92}La_{0.08}(Zr_{0.65}Ti_{0.35})O_3$ and $(Bi_{0.5}Na_{0.5})_{0.915}$-$(Bi_{0.5}K_{0.5})_{0.05}Ba_{0.02}Sr_{0.015}TiO_3$ ceramics, respectively [29,32]. More recently, a maximum harvestable energy density per cycle of 7.8 J/cm^3 was also achieved in our 2-μm-$Pb_{0.97}La_{0.02}(Zr_{0.75}Sn_{0.18}Ti_{0.07})O_3$ AFE thick film, which was the largest reported value to date [33].

Combined above facts, both the huge ECE and giant harvested thermal-electrical energy density could be simultaneously obtained in AFEs because of large pyroelectric effect caused by their field-induced phase transition, which makes AFEs a promising candidate for cooling and thermal-electrical energy harvesting application. However, currently, the studies on ECE and energy harvesting in AFEs are rarely reported and thus it is necessary to do a further investigation systemically. In this work, 1.5-μm-thick $(Pb_{0.97}La_{0.02})(Zr_{0.95-x}Sn_xTi_{0.05})O_3$ films with three typical

chemical compositions were prepared, as shown in Fig. 1(c), which located in orthorhombic region for x=0.08, in tetragonal region for x=0.38, and in the morphotropic phase boundary (MPB) for x=0.20. The aim of this work is to investigate the effects of phase structure on ECE and energy harvesting performance of AFE materials. The advantages of thick films lie both in higher critical breakdown field like thin films and in larger volume like bulk ceramics.

2. Experimental procedure

$Pb_{0.97}La_{0.02}(Zr_{0.95-x}Sn_xTi_{0.07})O_3$ (PLZST, x=0.08, 0.20 and 0.38) thick films were prepared by a sol-gel method. Lead acetate trihydrate (99.5%, Sinopharm Chemical Reagent Company, China), lanthanum acetate (99.9%, Aldrich), tin acetate (Aldrich), titanium isopropoxide (97%, Aldrich) and zirconium isopropoxide (70%, Aldrich) were used as the starting raw materials. Glacial acetic (85%, Sinopharm Chemical Reagent Company, China), and deionized water were used as solvents. 20 mol% excess of lead acetate trihydrate was introduced to compensate the lead loss during annealing and to prevent the formation of pyrochlore phase in the films. The concentration of the precursor solution was 0.5 M. The conductive $LaNiO_3$ (LNO) films with a thickness of about 400 nm were chosen as bottom electrodes, which were prepared on Si (100) substrates by a wet chemistry method as described in Ref.34. The obtained LNO films showed a (100) growth orientation. After aged for 24 h, PLZST AFE films were deposited on $LaNiO_3$/Si(100) substrates through a multiple-step spin-coating technique. Each wet PLZST layer was spin coated at 3000 rpm for 40 s. In order to reduce the formation of cracks, each wet film was first dried at 350 ^oC for 10 min and subsequently pyrolyzed at 600 ^oC for 10 min. The spin-coating and heat-treatment were repeated several times to obtain the desired thickness. To prevent excessive lead loss and form pure perovskite phase, a capping layer of 0.4 M PbO precursor solution which was prepared from lead acetate trihydrate was deposited on the top of the PLZST film before it went through a final anneal at 700 ^oC for 30 min. The final thickness of the three PLZST AFE thick films was about 1.5 μm, determined from the cross-sectional images.

The microstructures of these AFE thick films were analyzed by X-ray diffraction (XRD Bruker D8

Advanced Diffractometer, German) and field-emission scanning electron microscopy (FE-SEM ZEISS Supra 55, German), respectively. For the electrical measurements, gold pads of 0.20 mm in diameter were coated on the film surface as top electrodes by using a DC sputtering method. The frequency and temperature-dependent dielectric properties of the films were measured by using a computer-controlled Agilent E4980A *LCR* analyzer. The bipolar polarization-electric field hysteresis (*P-E*) loops at 1 kHz and the leakage current characteristic of the film were measured by a Ferroelectric tester (Radiant Technologies, Inc., Albuquerque, NM) with a heated probe station. *P-E* loops were made roughly every 15 ^{o}C in the measurement temperature range on heating procedure. ECE and the thermal-energy harvesting performance of the films were calculated according to the *P-E* results.

3. Results and discussion

Fig. 2 shows the XRD patterns of PLZST thick films deposited on the (100)-oriented LNO/Si substrates after being annealed at 700 ^{o}C, which were recorded with a step of 0.02^{o} at a rate of 6^{o} min^{-1} within 2θ from 20^{o} to 60^{o}. For convenience, the diffraction peaks were indexed according to pseudo-cubic structure, rather than orthorhombic or tetragonal structure. Evidently, all the three samples crystallized into pure perovskite phase, as no evidence of secondary phase formation, such as pyrochlore, was detected. Moreover, all the three samples showed a very strong (100) and (200) diffraction peaks, indicating a highly (100)-oriented characteristic. In order to estimate the degree of the (100) orientation, the orientation factor α (defined as α=(100)/(I(100)+I(110)+I(111)) was introduced [35]. The calculated α value was 94%, 82%, and 88% for x=0.08, 0.20, and 0.38, respectively. Although there are a lot of factors that affect the textured growth of lead-based thin films, such as lead excess content, heat-treatment procedure, and the selected substrates, etc., the reason for the (100)-preferred growth of PLZST thick films in present work is due to the same (100)-orientation of LNO bottom electrodes and the small lattice mismatch. The similar work was also reported in other lead-based FE and AFE films deposited on LNO bottom electrodes [34, 36].

Fig. 3(a-c) show surface microstructures of the PLZST AFE thick films. Evidently, all the films display dense and uniform microstructure, and no micro-cracks or other micro-structural defects

were found in the films. This was ascribed to the two-step heat-treatment procedure for the thick film preparation. The average grain size was about 259, 308, and 341 nm for the PLZST thick films with x=0.08, 0.20, and 0.38, respectively, which was calculated by using the Nano Measurer software. The small difference in grain size would not cause the difference in electrical properties of these thick films. Fig. 3(d) shows the typical cross-sectional image of the thick films with x=0.08, which presents a compact, columnar-like structure. It indicates that the nucleation and growth of the crystals may initiate from the bottom electrode. The estimated thickness of the films is about 1.5 μm.

Frequency-dependent dielectric constant and dielectric loss of the AFE thick films are plotted in Fig. 4(a), which were measured at room temperature and over 1-1000 kHz. Within the measurement frequency range, the dielectric constant for the three samples was only slightly fluctuated, and gradually decreased with the increase of frequency, which was induced by the different response times for the various dipoles. The phase structure of the thick films shows a clear effect on their dielectric constant. As x increases from 0.08 to 0.38, the dielectric constant also gradually increases. For example, dielectric constant at 100 kHz was 315, 391 and 490 for x=0.08, 0.20 and 0.38, respectively. Generally, the dielectric constant of AFE materials has a close relationship with the stability of AFE phase. Namely, higher stability of the AFE phase usually leads to lower dielectric constant. Based on previous report [37], AFEs in orthorhombic phase are more stable than that in tetragonal phase. Thus, in the present work, as tin content in the thick films increases leading to their structure change from orthorhombic to tetragonal phase, accordingly their dielectric constant increases. Different from their dielectric constant, all the thick films show the similar dielectric loss. The loss tangent is less than 0.02 at the frequency below 100 kHz, and greatly enhances at the frequency above 100 kHz. The large loss tangent values at high measurement frequency are often observed in AFE and FE films with oxide electrodes such as LNO, which is caused by the larger resistance of this kind of electrodes. In order to explain the resistance of electrode-dependent dielectric behavior, a proper three-component equivalent model was developed in our previous work [38].

Temperature dependences of the dielectric constant for PLZST AFE thick films are presented in Fig. 4(b), which were measured at 100 kHz on heating process. Clearly, all the AFE thick films with different compositions show only one dielectric peak during the heating process and no other phase transformation is observed. The dielectric constant in the all cases first increases gradually, and then decreases with the temperature increasing. The dielectric peaks corresponding to the transition from AFE to PE phase are observed at 215 ^{o}C, 187 ^{o}C, and 158 ^{o}C for x=0.08, 0.20, and 0.38, respectively, which correspond to the so-called Curie temperature (T_c). As shown in the insert in Fig. 4(b), T_c of the thick films is linearly shifted to low temperature as x value increasing, which further demonstrated that the stability of AFE phase is weaken by the addition of tin.

Room temperature *P-E* loops of the samples are shown in Fig. 5(a), which were measured at 1 kHz. Clearly, all the thick films exhibit double loops, demonstrating their AFE character. A small remnant polarization of below 8 μC/cm^2 was detected in the all samples, which should be caused by the interface layer, space charge, unstable AFE regions, and so on [39]. As x increases from 0.08 to 0.38, the *P-E* loops show a change from "squared" shape to "slanted" shape, indicating the reduced AFE stability of the thick films with higher tin content. Moreover, the chemical composition of the thick films also has a strong effect on their maximum polarization. Under the measurement condition, the corresponding maximum polarization for the films with x=0.08, 0.20 and 0.38 is 82.4, 74.6 and 54.5 μC/cm^2, respectively. This result illustrates that the polarization behavior of AFEs is related with their phase structure. Under sufficient high external electric field, AFE materials with orthorhombic structure possess larger maximum polarization value than AFEs materials with tetragonal structure. In another word, stable AFE phase usually leads to a larger maximum polarization value. The same result was also reported in AFE bulk ceramics and films with different phase structure [40, 41]. In order to study the ECE and energy harvesting performance of these AFE thick films, the pyroelectric coefficients at selected *E*, $\left(\frac{\partial P}{\partial T}\right)_E$ were deduced from fourth-order polynomial fits to raw *P(T)* data extracted from the upper branches of *P-E* loops at 900 kV/cm in $E > 0$. As showed in the insert in Fig. 5(a), all the films display large pyroelectric coefficient values at the selected *E*

with a magnitude of ~10^{-6} μC/K·cm^2, which are consistent with the reported values in AFEs [16]. Moreover, with the temperature increasing, the values of $\left(\frac{\partial P}{\partial T}\right)_E$ decrease gradually near room temperature, and then a peak is observed at higher temperature. The variation of the pyroelectric coefficient is resulted from the phase transition of the AFE thick films caused by electric field and temperature, which is explained in details in the following part. The corresponding *P-E* loops were measured at 25 °C, 35 °C, 45 °C, 60 °C, 150 °C, 160 °C, 170 °C, 180 °C, and 190 °C, as shown in the Fig. 5(b).

According to Eq. (1), the reversible adiabatic temperature changes ΔT of the AFE thick films with different x values are plotted in Fig. 6 (a). The specific heat capacity C = 330 J·K^{-1}·kg^{-1} and the theoretical density ρ = 8.3 g·cm^{-3} are selected for these thick films as reported before [9]. Here E_1 = 0 and $E_2 = E$; thus ΔE is equal to E. In the present work, applied field E is fixed at 900 kV/cm. As shown in the figure 6(a), the samples with x=0.08, 0.20, and 0.38 show the same changing tendency in the operating temperature-dependent ΔT curves. Clearly, as expected, the large ΔT are received in a wide range of near the room temperature, which is induced by the phase transition of FE-AFE. The values of ΔT at 25 °C are 13, 33, and 27 °C for x=0.08, 0.20, and 0.38, respectively. With the operating temperature increasing, the ΔT firstly decreases, indicating a reduction of entropy change between AFE and FE phase transition. With the further increase of temperature, a peak of ΔT = 8, 11, and 7 °C is detected at 185, 156, and 142 °C at E = 900 kV/cm, which is believed to be caused by the AFE-PE phase transition. The temperature corresponding to the peak of ΔT is slightly below its T_c, which is consistent with that previously reported by Tatsuzaki, because the spontaneous value of P greatly changes with temperature below T_c [42]. In fact, ECE can occur both above and below T_c, but the microscopic models of ECEs are not well established [9]. For the cooling application, apart from large ΔT, higher adiabatic entropy changes ΔS is also desired. Fig. 6(b) shows the corresponding adiabatic entropy changes ΔS of these PLZST AFE thick films with different x values. The temperature dependence of ΔS is observed in the curves, which demonstrate that large entropy change could occur during the FE-AFE and AFE-PE phase transition. The maximum ΔS

value is obtained at 25 ^{o}C, which is 14.0, 36.9, and 30.6 $J \cdot K^{-1} \cdot kg^{-1}$ for x=0.08, 0.20, and 0.38, respectively. These values are very close to the results reported in $Pb(Mg_{1/3}Nb_{2/3})_{0.65}Ti_{0.35}O_3$ thin film (32 $J \cdot K^{-1} \cdot kg^{-1}$) and FE polymer [P(VDF-TrFE)] (55/45 mol%) films (60 $J \cdot K^{-1} \cdot kg^{-1}$) [43,44]. Based on the results illustrated in Fig. 6, it can be clearly found that ECE is strongly dependent on the phase structure of the thick films. The phase structure-dependent cooling performance could be explained by following two reasons [45]. Firstly, it is generally accepted that the entropy change against the applied electric field is related to the number of the polar states in one dielectric [45]. It was reported that maximum ECE could be obtained in the polar materials with a chemical composition located near a muilt-phase coexisted point, such as $Ba(Ti_{1-x}Zr_x)O_3$, $(Ba_{1-x}Sr_x)TiO_3$, and $Ba(Ti_{1-x}Sn_x)O_3$ [46-48]. Thus, the largest ECE was obtained in the PLZST films with x=0.20, which is located in MPB of orthorhombic and tetragonal phase. Secondly, a smaller energy barrier for switching between the different polar states would produce a larger ECE under the application of electric field. It is well known that the energy barrier for AFE-FE switching of the tetragonal AFEs is lower than that of the orthorhombic AFEs. As a result, the tetragonal thick films with x=0.38 possess a larger ECE, in contrast to the orthorhombic films with x=0.08.

In order to provide a criteria for comparison for the electrocaloric refrigeration, the coefficient of performance (*COP*) is given and defined as the relationship between the isothermal heat Q and J, expressed as [49]:

$$COP = \frac{|Q|}{|J|} = \frac{|\Delta S \times T|}{J} \tag{4}$$

where Q is isothermal heat and J is the corresponding electrical work per unit volume and equal to $\int_{P_r}^{P_{max}} EdP$. Based on this formula, *COP* values for the PLZST thick films with different x content are shown in Fig. 7, the similar variation tendency of *COP* against temperature is also observed in these AFE thick films. The corresponding maximum *COP* values were also obtained at 25 ^{o}C and are 2.9, 5.9, and 5.7 for x=0.08, 0.20, and 0.38, respectively. The large *COP* values indicate a higher cooling efficiency originated from FE-AFE switching. Moreover, to measure quantitatively how effective

an applied electric field ΔE in generating ECE in the thick films is, the ratio of $\Delta T/\Delta E$ referred to as the electrocaloric coefficient is introduced. The value of $\Delta T/\Delta E$ at 25 ^{o}C is 0.014, 0.037, and 0.030 K·cm/kV for x=0.08, 0.20, and 0.38, respectively, which is consistent with the reported best values in AFEs [7, 18].

According to the formula (3), the chemical composition-dependent thermal-electrical energy harvesting performance based on the bipolar *P-E* loops of the AFE thick films is studied by using the Olsen cycle. The harvested energy density W per cycle is plotted in Fig. 8(a), as a function of high temperature T_H. The low electric field E_L and high electric field E_H were selected as 300 and 900 kV/cm, and the low temperature T_L at 20 ^{o}C. As expected, the W values gradually increase in all cases, as T_H rising from 45 to 200 ^{o}C. A maximum W values of 3.6, 6.8, and 4.0 J/cm^3 are shown at 200 ^{o}C for x=0.08, 0.20, and 0.38, respectively. The effects of high electric field E_H on the harvested energy density W per cycle are given in Fig. 8(b), where T_L and T_H are fixed at 20 and 200 ^{o}C, and E_L at 300 kV/cm. As the increase of E_H, the values of W are also improved, indicating that higher operating field is favored to obtain larger harvested energy density. According to the results in Fig. 8, it could be found that the thermal-electrical energy harvesting performance is also strongly dependent on the phase structure of the thick films. The largest harvested energy density W is obtained in the films with x=0.20 located in MPB of orthorhombic and tetragonal phases, followed by the tetragonal and then orthorhombic films, which is contributed to their different pyroelectric coefficient $\left(\frac{\partial P}{\partial T}\right)_E$, as shown in the insert in Fig. 5(a). The larger W values demonstrate that AFEs is a promising candidate for thermal-electrical energy harvesting.

Fig. 9(a) gives the W values per cycle of these AFE films as a function of T_L, with E_L=300 kV/cm, E_H=900 kV/cm, and fixed ΔT ($\Delta T=T_H-T_L$) of 80 ^{o}C. Clearly, the W values firstly decrease, and then a peak forms, as T_L increasing. This result could also be explained by the enhanced pyroelectric effect by electric field, caused by AFE-FE phase transition at low temperature and AFE-PE phase transition near its T_c [33]. For the thermal-electrical energy harvesting, apart from energy density, large energy efficiency (η) is also desired, which defined as [24]

$$\eta = \frac{W}{Q}, \tag{5}$$

where Q is the absorbed heat per cycle and equal to $C(T_H\text{-}T_L)$. C is the heat capacity of the material defined in formula (1). As shown in Fig. 9(b), the η value is improved, as T_H increasing. The maximum η values achieved at 200 ^{o}C are about 0.30%, 0.54%, and 0.32% for x=0.08, 0.20, and 0.38, respectively, which are consistent with the reported results [50, 51]. These results illustrate that enhanced thermal-electrical energy harvesting density and energy efficiency could be simultaneously obtained in the films with larger pyroelectric effect.

Regardless of cooling devices or thermal-electrical energy heaversing, a low leakage current in the dielectrics under the application of electric field is always desired in order to reduce to energy loss. Fig. 10(a) shows the current-time characteristics for dielectric relaxation current of the PLZST AFE thick films with different x values, which were measured at room temperature and 600 kV/cm. The leakage current density shows strong initial time-dependence because of the dielectric polarization relaxation, which obeys the Curie-von Schweidler law as follows [52]:

$$J = J_s + J_0 \times t^{-n} \tag{5}$$

where J_s is the steady-state current density, J_0 a fitting constant, t the relaxation time in second, and n the slope of the log-log plot. The possible mechanisms are associated with the Curie-von Schweidler law: space charge trapping, relaxation time distribution and electrical charge hopping. By fitting the leakage current density data into Eq. 5, the steady-state leakage current density J_s is 2.9×10^{-6}, 1.4×10^{-6}, and 8.2×10^{-7} A/cm^2 for x=0.08, 0.20, and 0.38, respectively, as shown in the inset of Fig. 10(a). Obviously, as x value increasing, the leakage current in the thick films is slightly declined. The smaller leakage current is consistent with our previous reports on the lead-based AFE films [18,52], which yield negligible Joule heating (~ 10^{-5} K) and do not affect *P-E* results because currents of hundreds of μA are required to switch the measured polarizations at 1 kHz. As a typical example, the current density-time characteristics of the thick films for x = 0.20 are presented in Fig. 10(b), which was measured at the temperature range of 25-200 ^{o}C and at 600 kV/cm. The obtained steady-state leakage current density is 2.9×10^{-6}, 4.8×10^{-6}, 1.6×10^{-5} and 3.2×10^{-5} A/cm^2 at 25, 75,

150, and 200 ^{o}C, respectively. Clearly, the leakage current density of the sample is increased as temperature increasing, which is supposed to be caused by the thermionic Schottky emission [53]. The data could be fitted into the Arrhenius relationship [54]:

$$J_s = C\exp\left(-\frac{E_a}{kT}\right) \quad (6)$$

where C is a fitting constant, E_a the activation energy, k the Boltzmann constant. According to the fitting curve showed in the inset of Fig. 10(b), the obtained activation energy is about 0.27 eV, which is close to the reported result in $Pb_{0.92}La_{0.08}(Zr_{0.52}Ti_{0.48})O_3$ films [53].

4. Conclusion

The phase structure dependence of cooling behavior and thermal-electrical energy harvesting performance was studied in $(Pb_{0.97}La_{0.02})(Zr_{0.95-x}Sn_xTi_{0.05})O_3$ AFE thick films with x=0.08, 0.20 and 0.38. Because of its larger pyroelectric effect in the thick films at x=0.20, the best results of both ECE and energy harvesting performance are simultaneously realized. Giant ECE values (ΔT=33 ^{o}C and ΔS=36.9 $J\cdot K^{-1}\cdot kg^{-1}$) were achieved at 25 ^{o}C in this AFE thick films during the FE-AFE switching, and the corresponding electrocaloric coefficient and refrigeration efficiency are 0.037 K·cm/kV and 5.9. By using the Olsen cycle, the largest thermal-electrical energy harvesting density W per cycle of 6.8 J/cm^3 is also obtained in the films with x=0.20, and the corresponding maximum energy efficiency is 0.54%. Moreover, a smaller leakage current was detected in these AFE thick films, which is favored to their applications. In summary, the results indicate that AFEs are promising candidates for both room-temperature cooling and thermal-electrical energy harvesting and that the performance could be optimized by the proper phase structure control.

Acknowledgements

The authors would like to acknowledge the financial support the Ministry of Sciences and Technology of China through 973-project under grant No.2014CB660811, the National Natural Science Foundation of China under grant No. 51462027, the Program for New Century Excellent

Talents in University (2012), and the Innovation Program of Inner Monglia University of Science and Technology No. 2014QNGG01.

Reference

[1] Lu, S. G.; Zhang, Q. M. Electrocaloric Materials for Solid-State Refrigeration. *Adv. Mater.* **2009**, *21*, 1983-1987.

[2] Scott, J. F. Electrocaloric Materials. *Annu. Rev. Mater. Res.* **2011**, *41*, 229-240.

[3] Valant, M. Electrocaloric Materials for Future Solid-state Refrigeration Technologies. *Prog. Mater. Sci.* **2012**, *57*, 980-1009.

[4] Li, X. Y.; Lu, S. G.; Chen, X. Z.; Gu, H. M.; Qian, X. S.; Zhang, Q. M. Pyroelectric and Electrocaloric Materials. *J. Mater. Chem. C* **2013**, *1*, 23-27.

[5] Bai, Y.; Han, X.; Qiao, L. J. Optimized Electrocaloric Refrigeration Capacity in Lead-free (1-x)$BaZr_{0.2}Ti_{0.8}O_3$-x$Ba_{0.7}Ca_{0.3}TiO_3$ Ceramics. *Appl. Phys. Lett.* **2013**, 102, 252904.

[6] Radebaugh, R.; Lawless, W. N.; Siegwarth, J. D.; Morrow, A. J. Electrocaloric Refrigeration at Cryogenic Temperatures. Ferroelectrics **1980**, *27*, 205-211.

[7] Thacher, P. D. Electrocaloric Effects of in Some Ferroelectric and Antiferroelectric Pb(Zr,Ti)O_3 Compounds. *J. Appl. Phys.* **1968**, *39*, 1996-2002.

[8] Tuttle, B. A.; Payne, D. A. The Effects of Microstructure on the Electrocaloric Properties of Pb(Zr,Sn,Ti)O_3 Ceramics. Ferroelectrics **1981**, *37*, 603-606.

[9] Mischenko, A. S.; Zhang, Q.; Scott, J. F.; Whatmore, R. W.; Mathur, N. D. Giant Electrocaloric Effect in Thin-film $PbZr_{0.95}Ti_{0.05}O_3$. Science **2006**, *311*, 1270-1271.

[10] Parui, J.; Krupanidhi, S. B. Electrocaloric Effect in Antiferroelectric $PbZrO_3$ Thin Films. *Phys. Stat. Sol. (RRL)* **2008**, *2*, 230-232.

[11] Wang, J. F.; Yang, T. Q.; Wei, K.; Yao, X. Temperature-electric Field Hysteresis Loop of Electrocaloric Effect in Ferroelectricity-direct Measurement and Analysis of Electrocaloric

Effect. I. *Appl. Phys. Lett*. **2013**, *102*, 152907.

[12] Bai, Y.; Han, X.; Cheng, X.; Qiao, L. J. Both High Reliability and Giant Electrocaloric Strength in $BaTiO_3$ Ceramics. *Sci. Rep*. **2013**, *3*, 2895.

[13] Kutnjak, Z.; Petzelt, J.; Blinc, R.; The Giant Electromechanical Response in Ferroelectric Relaxors As a Critical Phenomenon. *Nature* **2006**, *441*, 956-959.

[14] Neese, B.; Chu, B. J.; Lu, S. G.; Wang, Y.; Furman, E.; Zhang, Q. M. Large Electrocaloric Effect in Ferroelectric Polymers Neat Room Temperature. *Science* **2008**, *321*, 281-283.

[15] Li, Q.; Zhang, G. Z.; Zhang, X. S.; Jiang, S. L.; Zeng, Y. K.; Wang, Q. Relaxor Ferroelectric-based Electrocaloric Polymer Nanocomposites with a Broad Operating Temperature Range and High Cooling Energy. *Adv. Mater.,* DOI: 10.1002/adma.201405495.

[16] Xu, Z. K.; Zhai, J. W.; Chan, W. H.; Chen, H. Phase Transformation and Electric Field Tunable Pyroelectric Behavior of and Antiferroelectric Thin Films. *Appl. Phys. Lett*., **2006**, *88*, 132908.

[17] Corkovic, S.; Zhang, Q. Enhanced Pyroelectric Coefficient of Antiferroelectric-ferroelectric Bilayer Thin Films. *J. Appl. Phys*. **2009**, *105*, 061610.

[18] Zhao, Y.; Hao, X. H.; Zhang, Q. A Giant Electrocaloric Effect of $Pb_{0.97}La_{0.02}(Zr_{0.75}Sn_{0.18}Ti_{0.07})O_3$ Antiferroelectric Thick Films at Room Temperature. *J. Mater. Chem. C*, **2015**, *3*, 1694-1699.

[19] Bowen, C. R.; Taylor, J.; LeBoulbar, E.; Zabek, D.; Chauhanc, A.; Vaish, R. Pyroelectric Materials and Devices for Energy Harvesting Applications. *Energy Environ. Sci*. **2014**, *7*, 3817-4148.

[20] Sebald, G.; Guyomar, D.; Agbossou, A. On Thermoelectric and Pyroelectric Energy Harvesting. *Smart Mater. Struct,* **2009**, *18*, 125006.

[21] Clingman, W. H.; Moore, R. G. Application of Ferroelectricity to Energy Conversion Processes. *J. Appl. Phys*. **1961**, *32*, 675-781.

[22] Childress, J. D. Application of a Ferroelectric Materials in an Energy Conversion Device. *J. Appl. Phys*. **1961**, *33*, 1793-1798.

[23] Fatuzzo, E.; Kiess, H.; Nitsche, R. Theoretical Efficiency of Pyroelectric Power Converters, *J. Appl. Phys.* **1966**, *37*, 510-516.

[24] Olsen, R. B.; Bruno, D. A.; Briscoe, J. M. Pyroelectric Conversion Cycles. *J. Appl. Phys.* **1985**, *58*, 4709-4716.

[25] Olsen, R. B.; Evans, D. Pyroelectric Energy Conversion: Hysteresis Loss and Temperature Sensitivity of a Ferroelectric Material. *J. Appl. Phys.* **1982**, *54*, 5941-5944.

[26] Olsen, R. B.; Bruno, D. A.; Briscoe, J. M. Pyroelectric Conversion Cycle of Vinylidene Fluoride-trifluoroethylene Copolymer. *J. Appl. Phys.* **1985**, *57*, 5036-5042.

[27] Olsen, R. B.; Brown, D. D. High Efficiency Direct Conversion of Heat to Electrical Energy-related Pyroelectric Measurements. *Ferroelectrics* **1982**, *40*, 17-27.

[28] Chin, T. K.; Lee, F. Y.; Mckinley, I. M.; Goljahi, S.; Lynch, C. S.; Pilon, L. Driect Thermal to Electrical Energy Conversion Using 9.5/65/35 PLZT Ceramics in the Ergodic Relaxor Phase. *IEEE Trans. Ultrason. Ferroelectr. Freq. Control* **2012**, 59, 2373-2384.

[29] Lee, F. Y.; Goljahi, S.; Mckinley, I. M.; Lynch, C. S.; Pilon, L. Pyroelectric Waste Heat Energy Harvesting Using Relaxor Ferroelectric 8/85/35 PLZT and the Olsen Cycle. *Smart Mater. Struct.,* **2012**, *21*, 025021.

[30] Navid, A.; Lynch, C. S.; Pilon, L. Purified and Porous Poly(vinylidene fluoride-trifluorothylene) Thin Films for Pyroelectric Infrared Sensing and Energy Harvesting. *Smart Mater. Struct.* **2010**, *19*, 055006.

[31] Zhu, H. Y.; Pruvost, S.; Guyomar, D.; Khodayari, A. Thermal Energy Harvesting From $Pb(Zn_{1/3}Nb_{2/3})_{0.955}Ti_{0.045}O_3$ Single Crystals Phase Transitions. *J. Appl. Phys.* **2009**, *106*, 124102.

[32] Vats, G.; Vaish, R.; Bowen, C. R. An Analysis of Lead-free $(Bi_{0.5}Na_{0.5})_{0.915}$-$(Bi_{0.5}K_{0.5})_{0.05}Ba_{0.02}Sr_{0.015}TiO_3$ Ceramic for Efficient Refrigeration and Thermal Energy Harvesting. *J. Appl. Phys.* **2014**, *115*, 013505.

[33] Hao, X. H.; Zhao, Y.; An, S. L. Giant Thermal-energy Harvesting Effect of $Pb_{0.97}La_{0.02}(Zr_{0.75}Sn_{0.18}Ti_{0.07})O_3$ Antiferroelectric Thick Film. *J. Am. Ceram. Soc.* **2015**, *98*, 361-365.

[34] Li, J. K.; Yao, X. Microstructure and Electrical Properties of $Pb(Zr_{0.52}Ti_{0.48})O_3$ Ferroelectric Films on Different Bottom Electrodes. *Mater. Lett.*, **2004**, *58*, 3447-3450.

[35] Hao, X. H; Zhai, J. W. Improved Dielectric Properties of (110)-preferred (Pb,La)(Zr,Sn,Ti)O_3 Antiferroelectric Thin Films on Metalorganic Decomposition Derived $LaNiO_3$ Buffer Layer. *J. Cryst. Growth*, **2008**, *311*, 90-94.

[36] Zhai, J. W.; Li, X.; Yao, Y.; Chen, H. Growth and Characterization of PNZST Thin Films. *Mater. Sci. Eng., B*, **2003**, *99*, 230-233.

[37] Hao, X. H; Zhai, J. W.; Kong, L. B.; Xu, Z. K. A Comprehensive Review on the Progress of Lead Zirconate-based Antiferroelectric Materials. *Prog. Mater. Sci.*, **2014**, *63*, 1-57.

[38] Hao, X. H; Zhai, J. W.; Jia, Q. P.; Shen B.; Yao, X. Temperature and Frequency Dependent Electrical Properties of (Pb,La)(Zr,Sn,Ti)O_3 Antiferroelectric Thin Films on $LaNiO_3$ Bottom Electrode with Different Sheet Resistance. *J. Phys. D: Appl. Phys.*, **2008**, *41*, 165403.

[39] Wang, Y.; Hao, X. H; Xu, J. B. Effects of PbO-insert Layer on the Microstructure and Energy Storage Performance of (042)-preferred PLZT Antiferroelectric Thick Films. *J. Mater. Res.*, **2012**, *27*, 1770-1775.

[40] Pan, W. Y.; Zhang, Q. M.; Bhalla, A.; Cross, L. E. Field-forced Antiferroelctric-to-ferroelectric Switching in Modified Lead Zirconate Titanate Stannate Ceramics. *J. Am. Ceram. Soc.*, **2013**, *72*, 571-578.

[41] Hao, X. H.; Wang, Y.; Zhang, L.; Zhang, L. W.; An, S. L. Composition-dependent Dielectric and Energy-storage Properties in (Pb,La)(Zr,Sn,Ti)O_3 Antiferroelectric Thick Films. *Appl. Phys. Lett*. **2013**, *102*, 163903.

[42] Mitsui, T.; Tatsuzaki, I.; Nakamura, E. An Introduction to the Physics of Ferroelectrics. Gordon and Breach, Landon, 1976.

[43] Saranya, D.; Chaudhuri, A. R.; Parui, J.; Krupanidhi, S. B.; Electrocaloric Effect of PMN-PT Thin Films Near Morphotropic Phase Boundary. *Bull. Mater. Sci.* **2009**, *32*, 259-262.

[44] Peng, B. L.; Fan, H. Q.; Zhang, Q. A Giant Electrocaloric Effect in Nanoscale Antiferroelectric and Ferroelectric Phases Coexisting in a Relaxor $Pb_{0.8}Ba_{0.2}ZrO_3$ Thin Film at Room Temperature", *Adv. Funct. Mater.*, **2013**, *23*, 2987-2992.

[45] Qian , X. S.; Ye, H. J.; Zhang, Y. T.; Gu, H. M.; Li, X. Y.; Randall, C. A.; Zhang, Q. M. Giant Electrocaloric Response Over A Broad Temperature Range in Modifi ed $BaTiO_3$ Ceramics", *Adv. Funct. Mater.*, **2014**, *24*, 1300-1305.

[46] Liu, X. Q.; Chen, T. T.; Wu, Y. J.; Chen, X. M. Enhanced Electrocaloric Effects in Spark Plasma-sintered $Ba_{0.65}Sr_{0.35}TiO_3$-based Ceramics at Room Temperature. *J. Am. Ceram. Soc.*, **2013**, *98*, 1021-1023.

[47] Luo, Z. D.; Zhang, D. W.; Liu, Y.; Zhou, D.; Yao, Y. G.; Liu, C. Q.; Dkhil, B.; Ren, X. B.; Lou, X. J. Enhanced Electrocaloric Effect in Lead-free $BaTi_{1-x}Sn_xO_3$ Ceramics Near Room Temperature. *Appl. Phys. Lett*. **2014**, *105*, 102904.

[48] Ye, H. J.; Qian, X. S.; Jeong, D. Y.; Zhang, S. J.; Zhou, Y.; Shao, W. Z.; Zhen, L.; Zhang, Q. M. Giant Electrocaloric Effect in $BaZr_{0.2}Ti_{0.8}O_3$ Thick Film. *Appl. Phys. Lett*. **2014**, *105*, 152908.

[49] Defay, E.; Crossley, S.; Narayan, S. K.; Moya, X.; Mathur, N. D. The Electrocaloric Efficiency of Ceramic and Polymer Films. *Adv. Mater.* **2013**, *25*, 3337-3342.

[50] Olsen, R. B.; Briscoe, J. M.; Bruno, D. A.; Butler, W. F. A Pyroelectric Energy Converter Which Employs Regeneration. Ferroelectrics **1981**, *38*, 975-978.

[51] Olsen, R. B.; Bruno, D. A.; Briscoe, J. M. Cascaded Pyroelectric Energy Converter. Ferroelectrics **1981**, *59*, 205-219.

[52] Zhao, Y.; Hao, X. H.; Zhang, Q. Energy-storage Properties and Electrocaloric Effects of $Pb_{(1-3x/2)}La_xZr_{0.85}Ti_{0.1}5O_3$ Antiferroelectric Thick Films. *ACS Appl. Mater. & Interfaces,* **2014**, *6*, 11633-11639.

[53] Hu, Z. Q.; Ma, B. H.; Koritala, R. E.; Balachandran, U. Temperature-dependent Energy Storage Properties of Antifeorroelectric $Pb_{0.96}La_{0.04}Zr_{0.98}Ti_{0.02}O_3$ Thin Films. *Appl. Phys. Lett*., **2014**, *104*, 263902.

[54] Ma, B. H.; Chao, S.; Narayanan, M.; Liu, S. S.; Tong, S.; Koritala, R. E.; Balachandran, U. Dense PLZT Films Grown on Nickel Substrates by PVP-modified Sol-gel Method. *J. Mater. Sci*. **2013**, *48*, 1180-1185.

Figure Caption

Fig. 1 (a) Schematic drawing of the ECE process of AFEs upon withdrawal of external electric field, (b) The diagram of the thermal-electrical energy harvesting by using a typical pyroelectric material from the Olsen cycle, and (c) Phase diagram of $Pb_{0.97}La_{0.02}(Zr,Ti,Sn)O_3$ system.

Fig. 2 XRD patterns of the PLZST AFE thick films with x=0.08, 0.20 and 0.38.

Fig. 3 Surface FE-SEM images of the PLZST AFE thick films (a) x=0.08, (b) x=0.20, (c) x=0.38; (d) cross-sectional image of the thick films x=0.08.

Fig. 4 (a) Room temperature frequency-dependent dielectric constant and dielectric loss of the PLZST AFE thick films with x=0.08, 0.20 and 0.38, (b) the corresponding temperature-dependent constant of the films at 100 kHz. The insert gives x value-dependent Curie temperature of these films.

Fig. 5 (a) Room temperature *P-E* loops of the PLZST AFE thick films with x=0.08, 0.20 and 0.38. The insert shows the corresponding temperature-dependent pyroelectric coefficient of the films at 900 kV/cm, and (b) the *P-E* loops of the film with x=0.08 at different temperature.

Fig. 6 (a) Temperature change of ΔT as a function of temperature at 900 kV/cm of the PLZST AFE thick film with x=0.08, 0.20 and 0.38, and (b) the corresponding adiabatic changes in entropy ΔS of the films.

Fig. 7 The temperature dependence of the refrigeration efficiency at 900 kV/cm of the PLZST AFE thick film with x=0.08, 0.20 and 0.38.

Fig. 8 (a) Harvested energy density per cycle of the PLZST AFE thick films under a function of T_H, and (b) E_H-dependent harvested energy density per cycle.

Fig. 9 (a) T_L-dependent harvested energy density per cycle of the PLZST AFE thick films with x=0.08, 0.20 and 0.38, (b) harvested efficiency of these PLZST AFE thick films with respect to T_H.

Fig. 10 (a) Dielectric relaxation current and corresponding fitting curve of the PLZST AFE thick films with x=0.08, 0.20 and 0.38 at 600 kV/cm. The insert gives the corresponding steady-state leakage current density of the films. (b) The temperature-dependent dielectric relaxation current and corresponding fitting curve of the PLZST AFE thick films with x=0.20. The insert gives the corresponding steady-state leakage current density and corresponding fitting curve as a function of reciprocal temperature.

Fig. 1 Xihong Hao, and Ye Zhao, *et. al.*

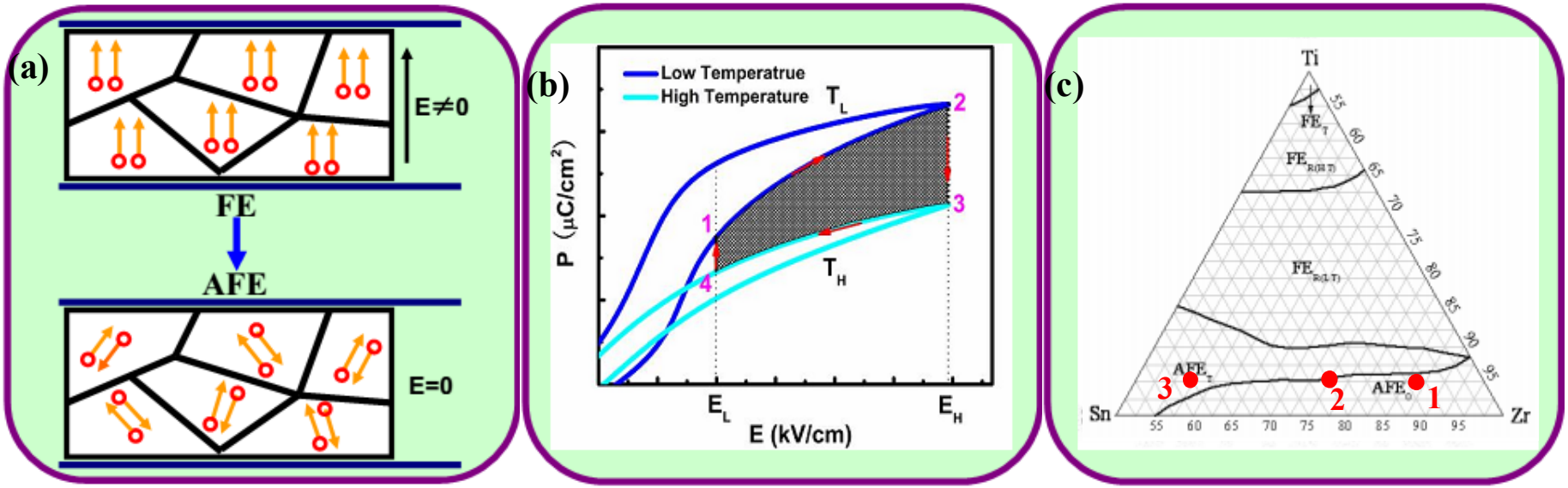

Fig. 2 Xihong Hao, and Ye Zhao, *et. al*

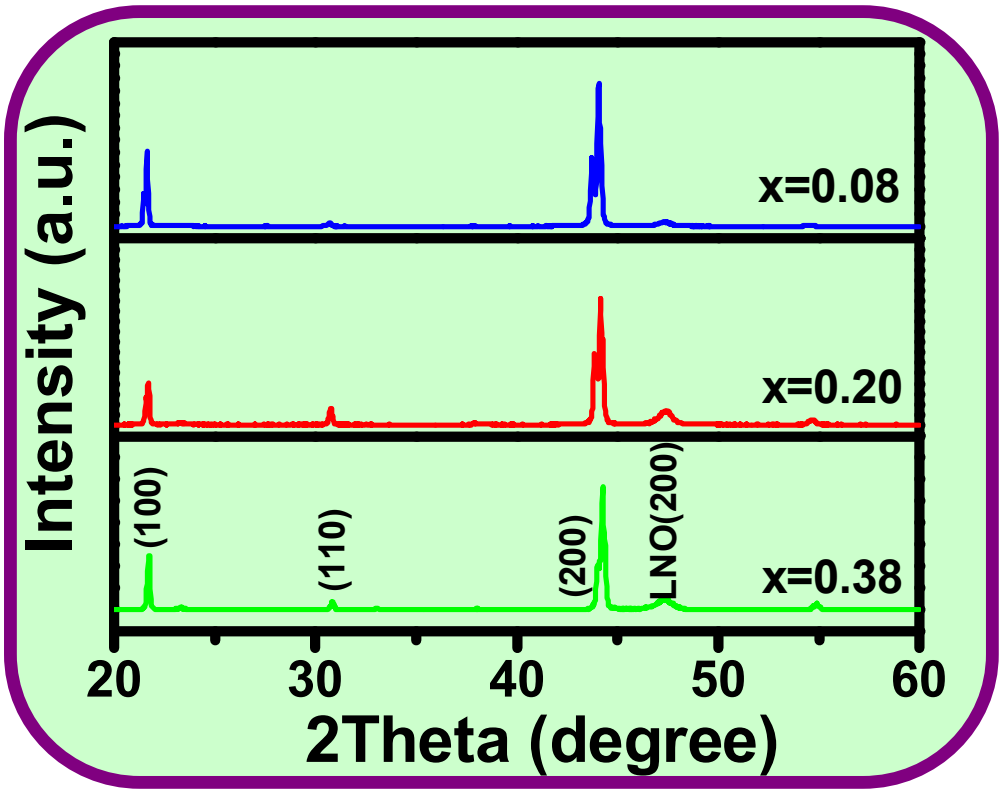

Fig. 3 Xihong Hao, and Ye Zhao, *et. al.*

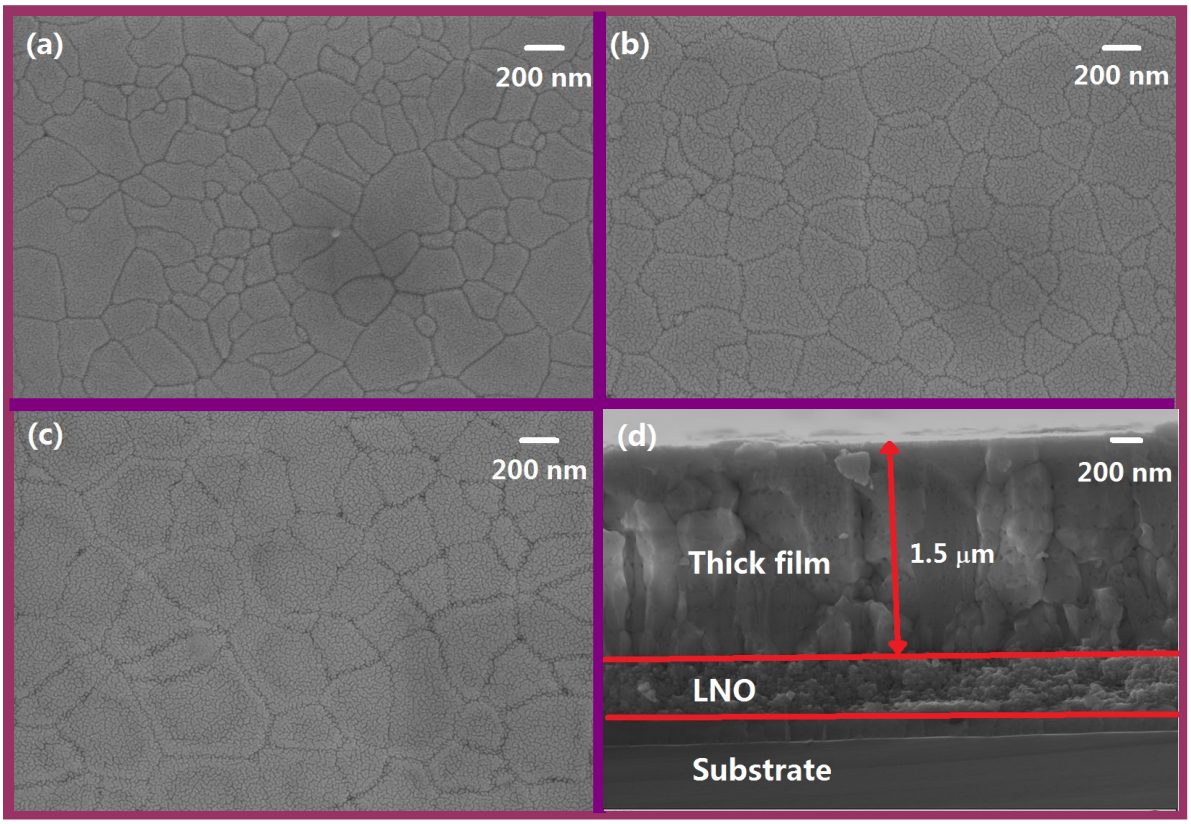

Fig. 4 Xihong Hao, and Ye Zhao, *et. al.*

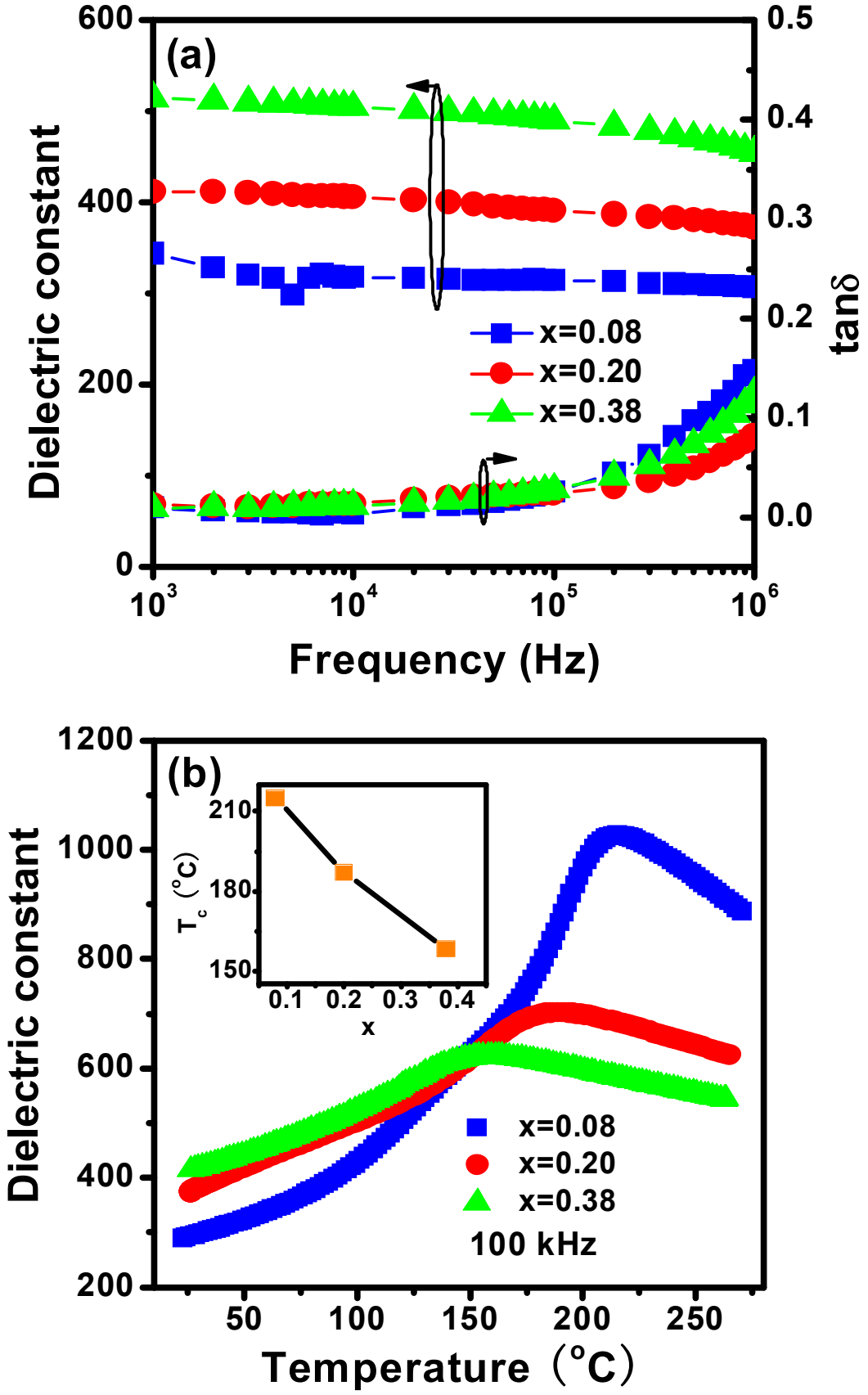

Fig.5 Xihong Hao, and Ye Zhao, *et. al.*

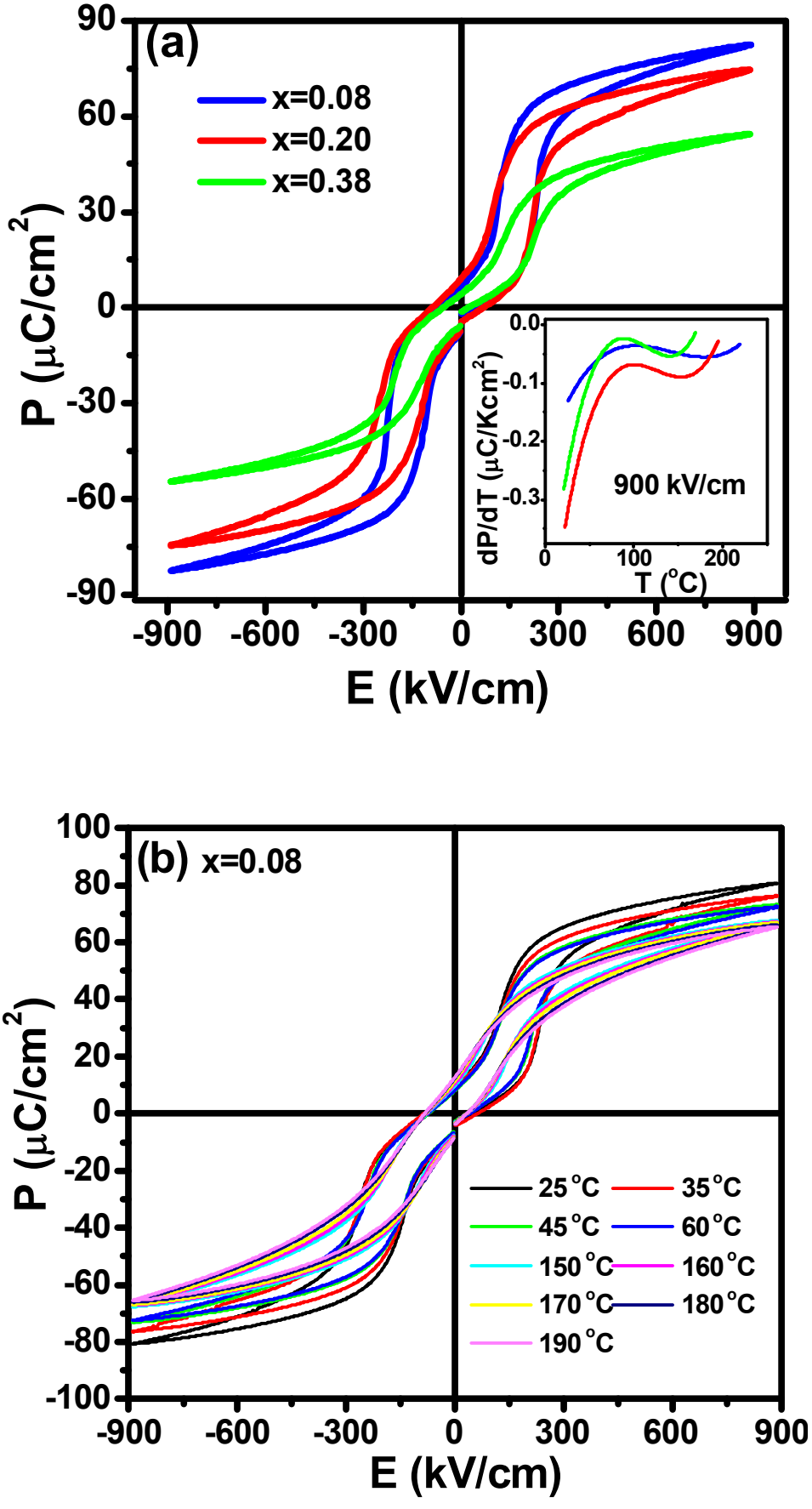

Fig. 6 Xihong Hao, and Ye Zhao, *et. al.*

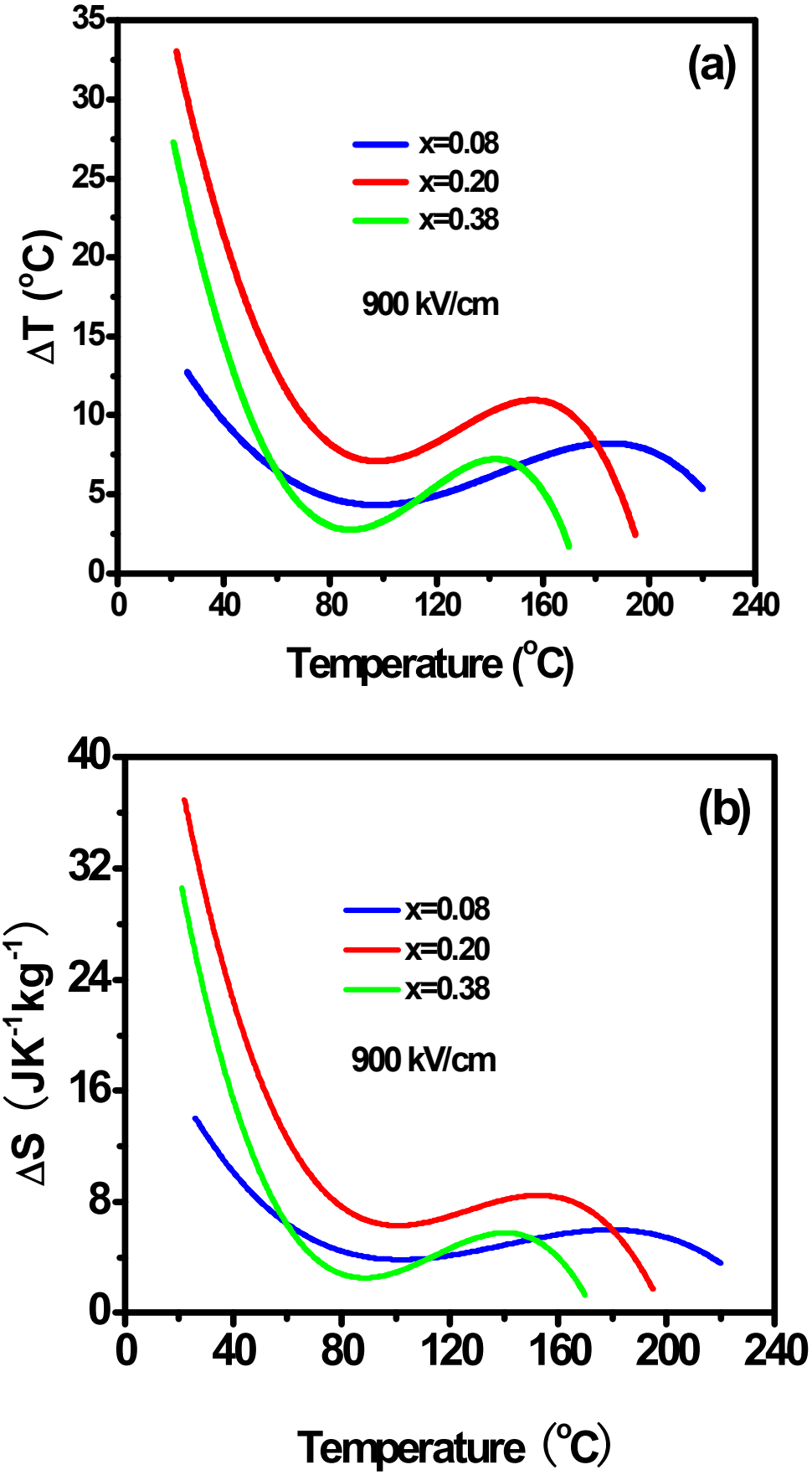

Fig. 7 Xihong Hao, and Ye Zhao, *et. al.*

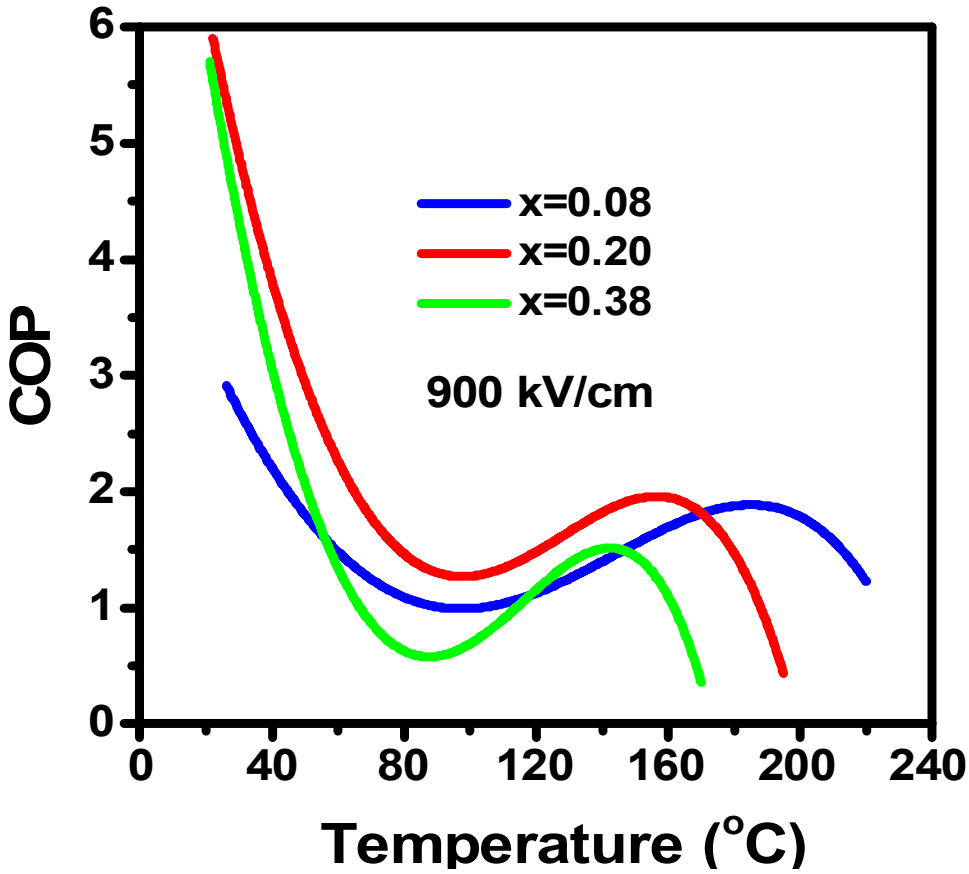

Fig. 8 Xihong Hao, and Ye Zhao, *et. al.*

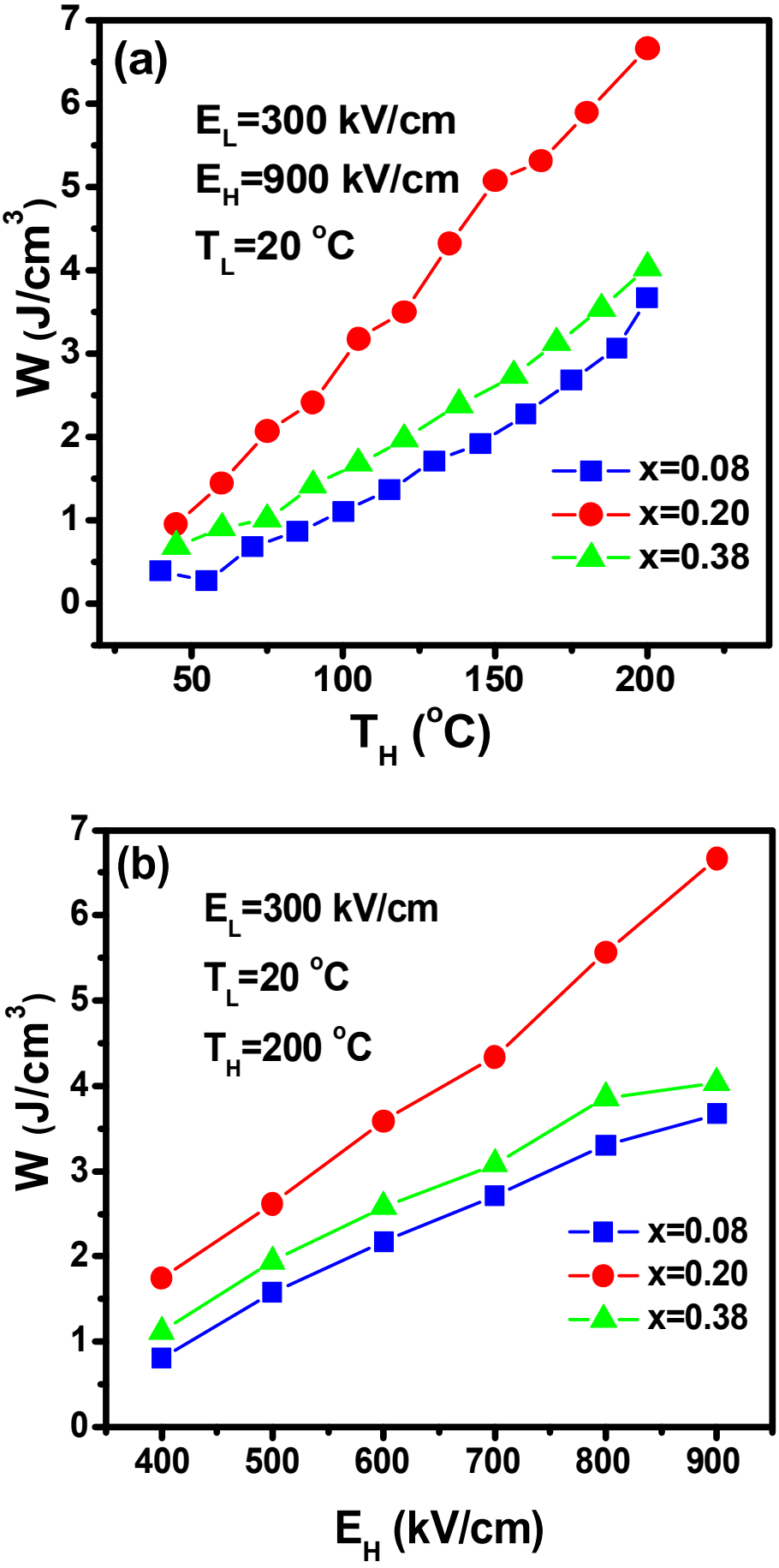

Fig. 9 Xihong Hao, and Ye Zhao, *et. al.*

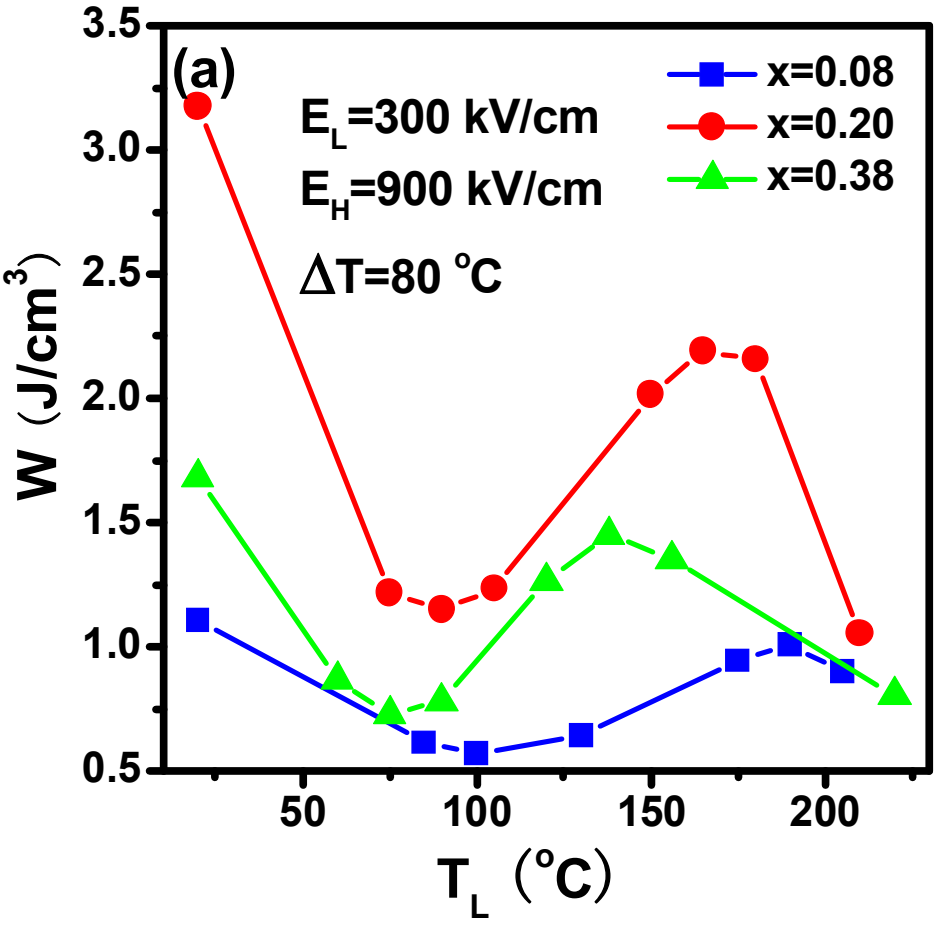

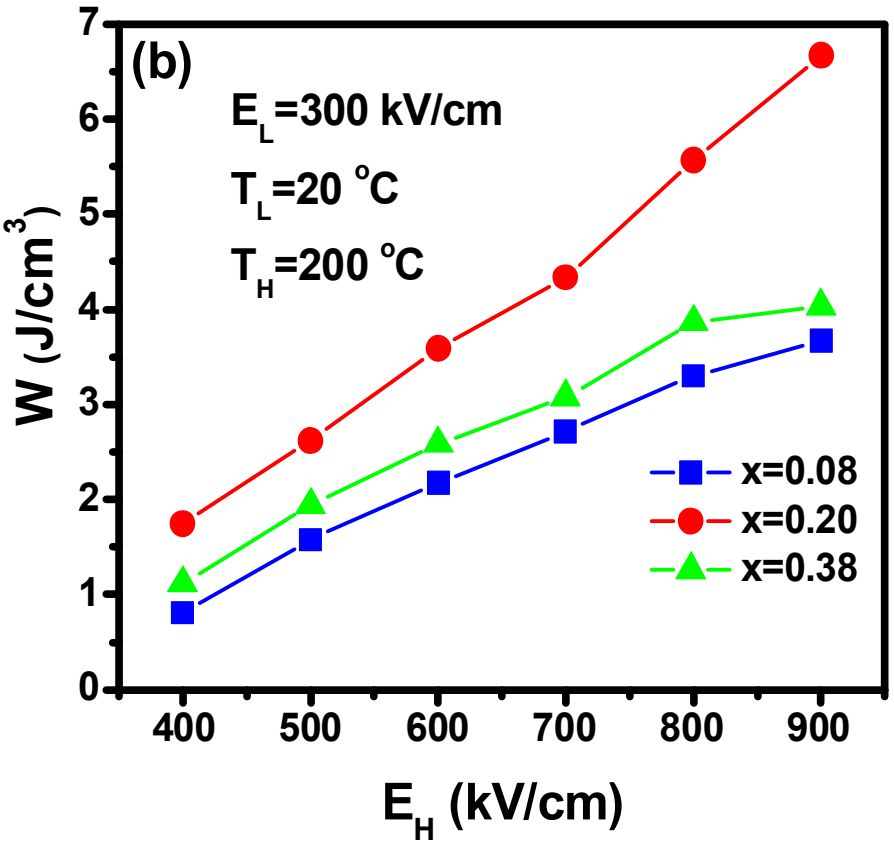

Fig. 10 Xihong Hao, and Ye Zhao, *et. al.*

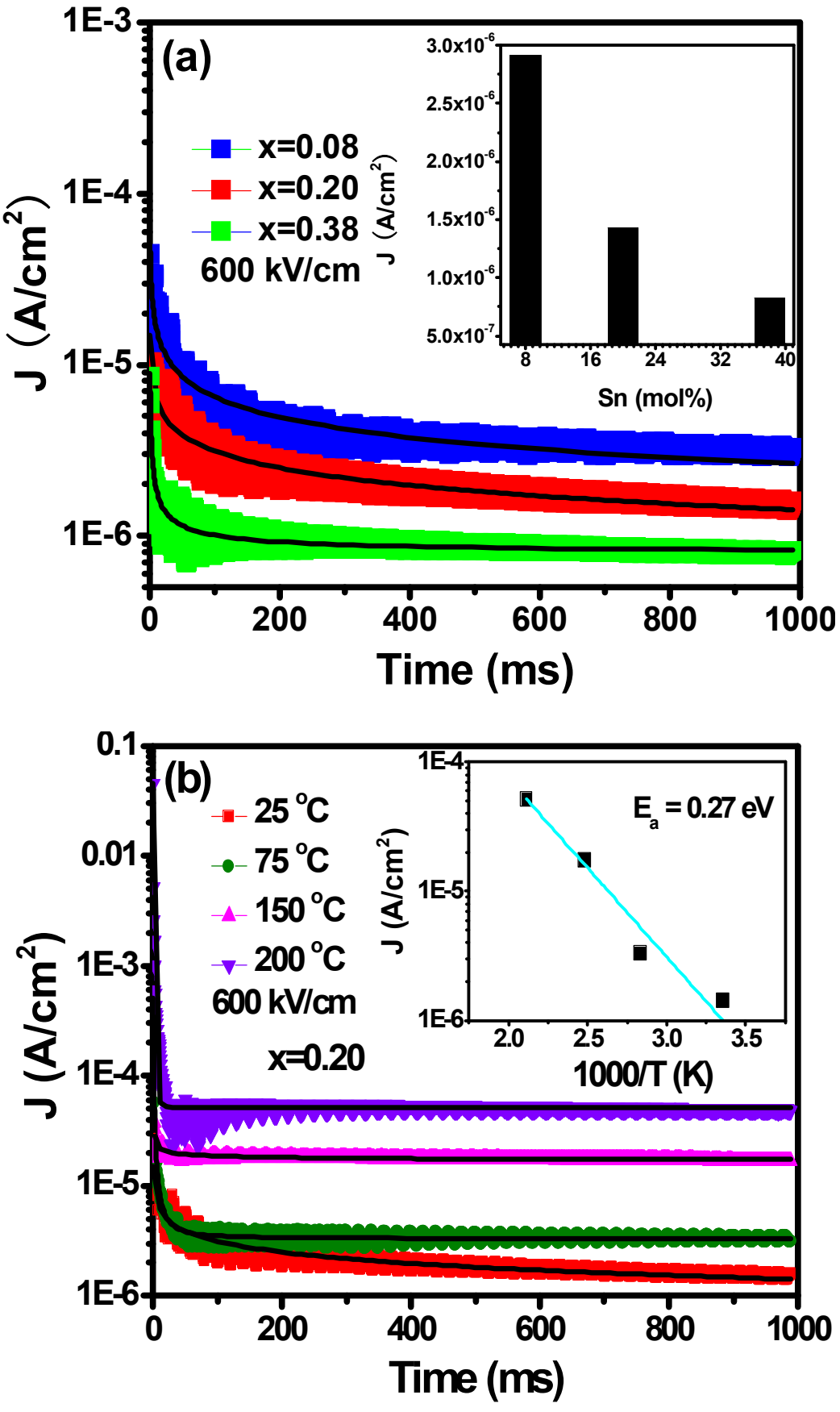

Table of Contents Graphic